A Mechanism of Real-Time Noise Modulation in Neurons

[1]Sharmila Venugopal[1], [1]Soju Seki, [5]David H Terman, [3]Antonios Pantazis, [3]Riccardo Olcese, [4]Martina Wiedau-Pazos, [1,2]Scott H Chandler*

[1]Department of Integrative Biology and Physiology
[2]The Brain Research Institute
[3]Departments of Anesthesiology & Perioperative Medicine and [4]Neurology
David Geffen School of Medicine, University of California Los Angeles

[5]Department of Mathematics
The Ohio State University

***Editorial and manuscript correspondence to SV**
Department of Integrative Biology and Physiology
University of California Los Angeles
621, Charles E Young Drive South, LSSA 4214
Los Angeles, CA 90095
Phone: (310) 206-0332
Email: vsharmila@g.ucla.edu

pages: 25 (including online methods section)
figures: 9
words in abstract: 159
words (Introduction, Results and Discussion): 3345
references: 36

Supplementary information included as one separate file: 4 figures, 1 table and Supplementary information including 2 pieces of model code, 3 pieces of dynamic-clamp C^{++} code, and, supplementary text detailing relevant theoretical analyses.

Author contributions: SV designed the study and conducted mathematical modeling and simulations with inputs from SHC; DHT and SV performed mathematical analyses; SS conducted *in vitro* patch-clamp electrophysiology and SV and SHC provided supervision; SS and AP performed the dynamic-clamp experiments with inputs from SV and RO provided supervision; AP implemented the Markov model and SV tested it; MWP generated the mice for the study; SV made the figures and wrote the manuscript; All the authors contributed to the final version.

Additional Information

Competing Interests
The authors declare no competing interests.

Uncertainties pose an ongoing challenge for information processing in the nervous system. It is not entirely clear how neurons maintain dynamic stability of information, encoded in the temporal features of spike trains, notwithstanding stochastic influences. Here we examined the contribution of subclasses of membrane sodium currents in real-time noise modulation in sensory neurons. Fast sodium (Na^+) currents are essential for spike generation, and a persistent Na^+ current can entrain preferred input frequencies via membrane resonance. Using mathematical modeling, theory and experiments, we show that a resurgent Na^+ current can stabilize the temporal features of burst discharge and confer noise tolerance. These novel insights reckon the role of biophysical properties of Na^+ currents beyond mere spike generation. Instead, these mechanisms might be how neurons perform *real-time* signal processing to maintain order and entropy in neural discharge. Our model analysis further predicts a negative feedback loop in the molecular machinery of an underlying Nav1.6-type Na^+ channel gating considered in this study.

Real-time signal detection in uncertain settings is a fundamental problem for information and communication systems. Our nervous system performs the daunting task of extracting meaningful information from natural environments and guides precise behaviors in *real-time*. Sensory neurons for instance use efficient coding schemes such as bursting that aid information processing [1]. Mathematical models of bursting have helped explain the basic structure of an underlying dynamical system as one in which, a slow process dynamically modulates a faster spike-generating process, leading to stereotypical alternating phases of spiking and quiescence [2, 3]. The so-called *recovery period* of the slow process governs the intervals between bursts which is often susceptible to random perturbations. Uncertainty in spike/burst intervals can alter the timing precision and information in a neural code[4]. Consequently, a mechanism that can control the refractoriness of spike and burst intervals notwithstanding stochastic fluctuations, may maintain order in neural spike trains and aid information processing. Here we examined a candidate mechanism involving neuronal voltage-gated Na^+ currents for a role in stabilization of burst discharge (durations and intervals), that can be important for real-time noise modulation.

Voltage-gated Na^+ currents are compulsory for spike generation in neurons. The molecular and structural diversity of Na^+ channels and the resultant functional heterogeneity and complexity, suggest their role beyond mere spike generation [5]. For instance, in addition to the fast/transient Na^+ current (I_{NaT})

mediating action potentials, a subthreshold activated persistent Na^+ current (I_{NaP}) participates in the generation of subthreshold membrane oscillations (STO) (e.g., see[6]). These oscillations can lead to membrane resonance by which, a neuron produces the largest response to oscillatory inputs of some preferred frequency [7, 8]. Neurons utilize this mechanism to amplify *weak* synaptic inputs at resonant frequencies [9]. The slow inactivation and recovery of I_{NaP} further provides for the slow process required for burst generation [10] and therefore contributes to efficient information processing in multiple ways. However, during ongoing activity, random fluctuations can alter the precision and order of bursts, that can distort/diminish the information in neural code. Here, we provide evidence that a frequently observed Na^+ resurgent current (I_{NaR}) known to arise from an unusual open-channel unblocking of sodium channels [11], might be a mechanism by which neurons arbitrate uncertainty and maintain order in spike trains. Some Na^+ channels such as the Nav1.6-type mediate all the three currents, namely, I_{NaT}, I_{NaP}, and I_{NaR} and here we show that these biophysical properties can confer *real-time* signal processing capacity to neurons.

Results

A workflow including the approaches that we used to examine the contribution of biophysical properties of a neuron in shaping its signal processing capacity, is shown in **Fig. 1**. First, using mathematical modeling we assembled the known biophysical properties of Nav1.6-type Na^+ currents using a conductance-based Hodgkin-Huxley formalism[12]; we incorporated the model conductances into a realistic neuron model and were able to reproduce experimentally observed stereotypical bursting (**Fig. 1a**). To test the effects of the model Na^+ currents in real neurons and to validate our predictions, we used real-time closed-loop dynamic-clamp experiments in intrinsically bursting proprioceptive sensory neurons in the brainstem (**Fig. 1b**). Furthermore, model stability analyses, and uncertainty measurements were combined to explain the observed behaviors (**Fig. 1c**). Specifically, **Figs. 2** and **3** provide a description of the model I_{Na}, and its novel I_{NaR} component; **Figs. 4**, **5** and **6** show how I_{NaR} can exclusively modulate

burst refractoriness by a putative negative feedback loop in the Na^+ channel gating; **Figs. 7** and **8** provide evidence for I_{NaR}'s ability for real-time noise modulation. **Figure 9** sums up the workings of I_{NaR} and I_{NaP} and their co-contribution to signal processing in neurons.

We began by formulating a conductance-based model for the Nav1.6-type Na^+ currents. **Figure 2a** illustrates the total I_{Na} as a sum of the three components in our model: transient, I_{NaT}, resurgent, I_{NaR}, and, persistent, I_{NaP} currents. The classic I_{NaT} has fast inactivation, on the order of 1 ms. The novel I_{NaR} shows decay kinetics on the order of 10 ms, and the I_{NaP} shows slow inactivation and recovery, on the order of 1000 ms. We established the above formulation for I_{Na} with distinct conductances for the three components to permit examination of their exclusive contributions to neural dynamics, since these components are experimentally inseparable[13-15]. Given these macroscopic currents may arise from a single channel, we also implemented a state-based Markovian I_{Na} model [16] that does not dissociate the three components and ensured qualitative and quantitative similarities in the total I_{Na} during spiking in both models (see **Supplementary Fig. 1**). We further confirmed that our model I_{Na} satisfies the key contingencies of Na^+ channels carrying I_{NaR} (see **Supplementary Fig. 2**).

We incorporated the model I_{Na} into a conductance-based single-compartment neuron model (see schematic and membrane voltage trace in black in **Fig. 2b**). Together with a minimal set of Na^+, K^+ and a leak conductance, the model neuron faithfully reproduced the expected rhythmic burst discharge observed in proprioceptive brainstem Mesencephalic V (Mes V) sensory neurons; The I_{Na} generated during action potentials is shown in expanded time in the figure (red trace). **Figure. 2c** shows a real-time closed-loop dynamic-clamp experiment in an intrinsically bursting Mes V neuron. The control burst was generated by simply driving the neuron with a step depolarization, following which, we blocked action potential generation by bath application of tetrodotoxin (1 μM TTX) (see black horizontal bar in **Fig. 2c**). Subsequently, we introduced the model I_{Na} in real-time during TTX application and by adjusting the

conductances of the three I_{Na} components suitably, we were able to regenerate action potential bursts (see **Methods** on choice of conductance values); The dynamic-clamp I_{Na} generated during action potentials is shown in expanded time in the figure for comparison with the model simulation in **Fig. 2b** (red trace).

A novel formalism for resurgent Na^+ current

The total I_{Na} in our model has a novel resurgent component, I_{NaR}; the transient and persistent components are similar to our previous formalism [7]. **Figure 3a (left panel)** illustrates the proposed mechanism of Na^+ resurgence [16], wherein a putative blocking particle occludes an open channel following a brief depolarization such as during an action potential; subsequently during repolarization, a voltage-dependent unblock results in a resurgent Na^+ current. Our I_{NaR} formulation recapitulates this unusual behavior of Na^+ channels using nonlinear ordinary differential equations for a blocking variable (b_r) and a competing inactivation (h_r) (see **Methods**). The resultant macroscopic I_{NaR} is gated by the unblocking process represented by $(1 - b_r)$, wherein '1' represents all open channels and b_r reflects the proportion of channels in blocked state at any instant: the steady-state voltage dependency of unblock, $\left(1 - br_\infty(V)\right)$, and the competing inactivation ($hr_\infty(V)$), in the model are shown in **Fig. 3a (middle panel)**, along with the equation for I_{NaR}; the purple shaded region highlights the voltage-dependency of I_{NaR} activation during open-channel unblock. In **Fig. 3a (right panel)**, we show simulated I_{NaR} (in red), peaking during the recovery phase of spikes (in black). In **Fig. 3b (I.)**, we reproduced experimentally observed I_{Na} and highlight the resurgent component in both model (*left*) and experiment (*right*), (inset shows experimental protocol; also see legend and **Methods**). A comparative current-voltage relationship for the model and experiments is shown in **Fig. 3b (II.)**; also see **Supplementary Fig. 3** for detailed kinetics of model I_{NaR}.

Resurgent Na^+ and its control of spike and burst intervals

Given that I_{NaR} is activated during the recovery phase of an action potential, physiologically, any resulting rebound depolarization may control the spike refractory period, and increase spike frequency

135 and burst duration [17, 18]. We tested this by selectively increasing the maximal resurgent conductance g_{NaR}
136 in our model neuron simulation and in dynamic-clamp experiments as shown in **Figs. 4a** and **b**. We
137 quantified the inter-burst intervals (IBIs), burst duration (BD) and inter-spike intervals (ISIs) as shown in
138 **Fig.4c-e**. As expected, we noted that increasing g_{NaR}, reduced ISIs and increased BDs. Additionally, we
139 noted that, g_{NaR} increase resulted in longer IBIs (see red double arrows in **Figs. 4a**, **b** and **Fig. 4c**). This
140 was in contrast with the effects of the persistent Na^+ conductance, g_{NaP}, that *decreased* IBIs and had
141 negligible effects on ISIs as shown in **Fig. 5**; both currents increased the BDs (also see **Supplementary**
142 **Fig. 4** for g_{NaR} and g_{NaP} subtraction experiments showing consistent reverse effects).

143 The effects of persistent I_{NaP} in reducing IBIs can be explained by its sub-threshold activation[7],
144 wherein increasing g_{NaP}, can *promote* burst initiation and therefore reduce IBIs. Additionally, a high g_{NaP}
145 together with its slow inactivation helps maintain depolarization that can prolong BDs. Its effect on ISI is
146 negligible, because, once activated, its slow inactivation accumulates between spikes and does not
147 contribute to rebound depolarization during ISIs. Clearly, one effect that is not immediately obvious is an
148 increase in IBI due to increases in g_{NaR}. The intervals between bursts signify the recovery time of the
149 slow process underlying bursting activity. Our highly reproducible effect of g_{NaR} on IBIs in sensory Mes
150 V neurons using dynamic-clamp experiments and its qualitative and quantitative similarities with the
151 model prediction clarifies that this slow recovery process is indeed the slow inactivation/recovery variable
152 for I_{NaP} as in the model. As such, we examined the g_{NaR} mechanism of IBI control by further analyses of
153 the simulated membrane potential (grey traces) and the slow I_{NaP} inactivation/recovery variable (overlaid
154 magenta traces) of the model neuron under three conditions shown in **Figs. 6a-c**: 1) with control values
155 of g_{NaR} and g_{NaP} (**Fig. 6a**), 2) an increase in g_{NaP} compared to control (**Fig. 6b**), and, 3) an increase in
156 g_{NaR} compared to control (**Fig. 6c**). The peak and trough of the slow inactivation/recovery correspond to
157 burst *onset* and *offset* respectively. Comparing these traces in the three panels, we note that an increase in

158 g_{NaR} effectively *facilitated* the slow inactivation during a burst (see curvy arrow in **Fig. 6c** and legend).
159 This observation was further supported by estimations of theoretical thresholds for *burst onset* and *offset*
160 for increasing values of g_{NaR} (**Fig. 6d**) and, similar thresholds for increasing values of g_{NaP} are provided
161 for comparison in **Fig. 6e** (see legend and **Supplementary Information** for details). Note that changes in
162 g_{NaR} did not alter the burst onset thresholds, consistent with a lack of resurgent current before spike onset
163 (see brown arrow indicating burst onset threshold in **Fig. 6d**); Whereas, increasing g_{NaR}, consistently
164 *lowered* the burst offset threshold for the slow inactivation/recovery (see highlighted dashed box with
165 arrows pointing to the burst offset thresholds decreasing with increasing g_{NaR} values in **Fig.6d**). The net
166 effect is longer recovery time between bursts and therefore prolonged IBIs. Additionally, in **Fig. 6d**, an
167 increase in g_{NaR} extended the range of slow inactivation/recovery for which stable bursting regime exists
168 (marked by the green circles). This *gain in stability* is indicative of a *negative feedback loop* in the Na^+
169 channel gating mechanism. As shown in **Fig. 6f** (see boxed inset), during a burst, presence of channel
170 unblocking mechanism and the resulting resurgent Na^+ can facilitate slow channel inactivation, however,
171 increasing inactivation, eventually shuts off the unblocking events as more channels inactivate (see
172 arrows), and this terminates the burst. The schematic on the left summarizes a negative feedback loop
173 between the unblocking and slow inactivation processes of Na^+ channels.

174 **Burst refractoriness and noise tolerance offered by Na^+ currents**

175 During quiescence/recovery periods between bursts, the membrane voltage can be perturbed by
176 ambient noise and stochastic inputs, that can induce abrupt spikes and therefore disrupt IBIs. We reasoned
177 that the gain in stability of burst discharge due to g_{NaR} might be a mechanism for noise tolerance. To test
178 this, we introduced a broadband white Gaussian noise to disrupt the rhythmic burst discharge in the model
179 neuron when no g_{NaR} was present as shown in **Figs. 7a, b**. Subsequent addition of g_{NaR} indeed
180 significantly restored burst regularity (**Fig. 7c**). Model analyses in the (h_p, V) phase plane provides insight

into the mechanism of I_{NaR} mediated noise tolerance. Briefly, we project a portion of a (h_p, V) trajectory corresponding to the termination of one burst until the beginning of the next (see expanded insets in **Figs. 7a, b, c**) to the (h_p, V) diagrams shown in **Figs 7d, e, f** respectively (see **Supplementary Information** for details). In **Fig. 7d**, beginning at the magenta circle, the (h_p, V) trajectory (magenta trace) moves to the right as h_p recovers during an IBI, until a burst onset threshold is crossed; point where the blue circles meet the red and black curves (see **Supplementary Information** for details), and eventually bursting begins; see upward arrow marking a jump-up in V at the onset of burst. During a burst, while V jumps up-and-down during spikes, h_p moves to the left as slow inactivation accumulates during bursting (left arrow). Finally, when h_p reduces sufficiently, (h_p, V) gets closer to the burst offset threshold (points at which the green and blue circles meet), and the burst terminates (down arrow). *What is key in this figure* is that the IBI is well-defined as the time period in which the (h_p, V) trajectory moves along the red curve of steady states during the recovery process and moves past the burst onset threshold until a burst begins. However, when stochastic influences are present, the recovery period near-threshold is subject to random perturbations in V and can cause abrupt jump-up/spikes during the recovery period (see expanded inset in **Fig. 7b**). Projecting (h_p, V) during this period on to **Fig 7e**, we note that the near-threshold noise amplitudes can occasionally push the (h_p, V) trajectory (magenta) above a green region of attraction and this results in such abrupt spikes. Now, when g_{NaR} is added, the apparent restoration of burst regularity (see **Fig. 7c**) can be attributed to an expansion in this green shaded region as shown in **Fig. 7f** (see arrow pointing to a noise-tolerant region). In this situation, near-threshold random perturbations have less of an effect during the recovery process to induce abrupt spikes. *This way, I_{NaR} filters random perturbations at burst offset and in turn contributes to burst refractoriness.* We suggest that such a mechanism can offer dynamic stability to neural discharge by damping the effects of random perturbations that can alter the precision of bursts and therefore aid information processing.

204 **Resurgent Na^+ and burst entropy**

205 The spike/burst intervals, their timing precision and order are important for information coding [19-
206 23] . Given our prediction that I_{NaR} can offer noise tolerance and stabilize burst discharge, we examined
207 whether it can reduce uncertainty in spike/burst intervals and restore order in burst discharge. We tested
208 this using model simulations and also verified the predictions using real-time dynamic-clamp experiments
209 as shown in **Fig. 8a - d**. In both simulations and *in vitro* dynamic-clamp experiments, we disrupted the
210 inter-event intervals (IEIs) by adding a broadband white noise input in addition to a constant step
211 depolarization as shown by spike raster plots in **Figs. 8e** and **f**. Adding the g_{NaR} conductance successfully
212 restored the order of bursts. We used Shannon's entropy as a measure of uncertainty in IEIs and show that
213 increases in entropy up on noise addition could be reduced to control levels by addition of I_{NaR} as in **Fig.
214 8g** (see **Methods**). We also quantified the Coefficient of Variation (CV) and note that adding noise which
215 primarily reduced burst intervals, indeed decreased the CV, due to reduced standard deviation (s.d.) of the
216 IEI distribution. Subsequent addition of I_{NaR}, which significantly lengthened the IBIs, resulted in
217 increases in CV values due to an increase in IEI s.d. Taken together, we suggest that I_{NaR} can serve an
218 important role in information processing through its contribution to maintaining order and precision of
219 spike/burst intervals in *real-time*.

220

221 **Discussion**

222 Using a unique combination of mathematical modeling, simulations, theory and real-time closed-
223 loop experiments, we demonstrate a novel consequence of complex Na^+ currents in burst control, noise
224 modulation and information processing in sensory neurons. While the subclasses of Na^+ currents presented
225 here are experimentally inseparable, our unique and simplified modeling approach combined with *in silico*
226 *knock-in* of each Na^+ current component in closed-loop dynamic-clamp experiments, allowed examination

227 of their individual contributions in shaping the neural discharge. Additionally, theoretical analyses
228 revealed a putative negative feedback loop in the Nav1.6-type Na^+ channel gating mechanism. These
229 results portend the apparent consequences on burst control and signal processing capacity of neurons when
230 these currents are present.
231

232 **Stabilization of burst discharge and negative feedback loop in Na^+ channel gating**

233 In contrast with I_{NaP}, which drives near threshold behavior and burst generation, I_{NaR} facilitated
234 slow channel inactivation as bursts terminate (also note [10]). Increased channel inactivation due to I_{NaR} in
235 turn prolonged recovery from inactivation required to initiate subsequent burst of activity. Such an
236 interaction between open-channel unblock process underlying I_{NaR}, and, the slow inactivation underlying
237 I_{NaP}, offer a closed-loop *push-pull* modulation of IBIs, suggesting a negative feedback control of sodium
238 channel activity by resurgent and persistent mechanisms during ongoing bursts. Specifically, presence of
239 I_{NaR} facilitates slow Na^+ inactivation as shown by our theoretical analyses of model behavior; such
240 enhanced slow channel inactivation eventually shuts off channel opening and unblocking. This resulted
241 in stabilization of the burst structure and regulation of IBIs. Theoretically, this represents an enlarged
242 separatrix (or boundary) for transitioning from a sub-threshold non-spiking behavior to bursting behavior
243 (see enlarged green shaded region in **Fig. 7f**), and the neuron becomes refractory to burst generation. Such
244 burst refractoriness was also the basis for noise tolerance.

245 Is this apparent effect of I_{NaR} physiologically plausible? Biophysical studies indicate that recovery
246 from fast inactivation is facilitated in sodium channels that can pass resurgent current [16]; as shown here,
247 this appears to be true for slow inactivation as well. Consistently, in the SCN8a knockout Med mouse,
248 which lack the Nav 1.6 sodium channel subunit, recordings from mutant cells showed an absence of
249 maintained firing during current injections, limited recovery of sodium channels from inactivation, and

failure to accumulate in inactivated states. This is attributed to a significant deficit in I_{NaR} [10, 17, 24]. Furthermore, maintained or repeated depolarization can allow a fraction of sodium channels in many neurons to enter inactivation states from which recovery is much slower than for normal fast inactivation (reviewed in [25]). Here, our simulations and model analyses predict that the presence, and increase in I_{NaR} conductance, provides for a such a physiological mechanism to maintain sustained depolarization and promote fast and slow channel inactivation.

Sodium currents and signal processing in neurons

Neuronal voltage-gated Na^+ currents are essential for action potential generation and propagation, a mechanism explained by the classic Hodgkin-Huxley model[12]. However, to enable fight-or-flight responses, an overt spike generation mechanism must be combined with *real-time* filters to extract biologically relevant inputs from an uncertain input space. Here we show that, the complex biophysical properties of Na^+ channels, can serve a role in *real-time* signal processing. A sub-threshold activated persistent Na^+ current is known to contribute to membrane resonance, a mechanism of band-pass filtering of preferred input frequencies[8]. We call this type of input gating, which is widely known to be important for brain rhythms[8, 22], a *tune-in* mechanism. Stochastic influences such as ambient noise and synaptic activity, can heighten the efficacy of a tune-in mechanism by amplifying weak inputs and can indeed promote signal detection[26, 27]. Furthermore, the persistent Na^+ current is important for burst generation and therefore also contributes to efficient coding[28, 29]. Then again, a resurgent Na^+ current, that turns on during the repolarizing phase of an action potential, can facilitate further spike generation by providing an after-depolarization[17]. Here we show that this mechanism can stabilize burst duration and intervals and maintain order of burst discharge in the presence of stochastic inputs. During ongoing sensory processing, we think that this can provide for a real-time *tune-out* mechanism, which stabilizes the bursts encoded due

to a detected input signal. This indeed needs to be validated in the presence of natural stimuli. However, our model predictions, analyses and experimental validation based on a broadband noise and step input strongly supports such a putative role. As summarized in **Fig. 9**, sensory neurons can utilize these biophysical properties as a *real-time tune-in-tune-out* mechanism for gating preferred inputs and dynamically attenuate random membrane fluctuations which can decrease uncertainty in neural code[30].

Figure Legends

Figure 1. A workflow showing the study components and approaches. a) Development of a mathematical models for Nav1.6-type Na^+ current components. This is incorporated into a minimal conductance-based model for a bursting neuron to investigate putative roles for these currents in neural dynamics. **b)** Model predictions are iteratively validated using real-time closed-loop dynamic-clamp experiments in brainstem proprioceptive sensory neurons. **c)** The observed effects on neural discharge are explained using theoretical stability and uncertainty analyses.

Figure 2. Ionic conductance-based model for Nav1.6 type Na^+ currents with three components. a) A simulated trace showing I_{Na}; the tree map shows each of the three components: transient I_{NaT}, resurgent I_{NaR}, and, persistent I_{NaP}; These are also highlighted by the color-matched dashed boxes in the top panel. The τ_{decay} shows the order of magnitude of the decay kinetics of the three components. **b)** *Left:* A schematic showing a conductance-based minimal model for a bursting neuron with the I_{Na} incorporated; also shown are potassium (I_K) and leak (I_{leak}) conductances in the model. *Right:* Model simulation demonstrates rhythmic burst discharge and inset highlights the I_{Na} current in the model during action potentials, in red. **c)** *Left:* Schematic shows the dynamic-clamp experimental approach in neurons in the brainstem proprioceptive sensory nucleus (red) in a live brain slice preparation; V_m, indicates the membrane potential. *Right*: Membrane potential recorded from a rhythmically bursting sensory neuron; action potentials were blocked using 1μM TTX, and dynamic-clamp model I_{Na} was applied to regenerate spikes; double slanted lines indicate break in time; Inset highlights the dynamic-clamp I_{Na} in red, during action potentials.

Figure 3. A novel mathematical model for the unusual resurgent component of the Nav1.6-type Na^+ current. a) *Left:* Schematic of voltage-dependent of state transitions for a Na^+ channel with a known mechanism of unusual open-channel block/unblock (green circle); classic inactivation gate is shown in blue (blue ball and chain). *Middle:* The steady-state voltage-dependencies of open-channel unblocking $(1 - br_\infty(V))$ and a competing inactivation process $hr_\infty(V)$ for the novel resurgent component are shown (also see Methods and Results); The purple shaded region highlights the voltage range over which I_{NaR} can be observed during open-channel unblocking. The equation for I_{NaR} is shown with the blocking (b_r), and, inactivation (h_r) gating variables (also see Methods). *Right:* The simulated I_{NaR} (in magenta) with

peaks occurring during the repolarization phase of action potentials (in black) is shown. **b) I.** A comparison between simulated I_{Na} and experimentally generated I_{Na} from voltage-clamp recording is shown; Boxed inset shows the experimental protocol typically used to test for voltage-dependent activation of I_{NaR}. **II.** Graphs show the nonlinear current-voltage relationship of peak resurgent current in the model (magenta) and average peak resurgent currents measured from voltage-clamp experiments (black); error bars show standard deviation (n=5 neurons from 5 animals).

Figure 4. Physiological consequences of I_{NaR} on neural discharge. a) Simulated membrane voltage for increasing values of g_{NaR}, and its effect on burst discharge. Value of 1x g_{NaR} adjusted to match experimental data in **(b)**. **b)** Dynamic-clamp addition of I_{NaR} in an intrinsically bursting sensory neuron and its response to increases in g_{NaR}; Values of g_{NaR} used are 2 and 4 nS/pF for 1X and 2X respectively. The red double arrows highlight increases in inter-burst interval (IBI) in both **(a)** and **(b)**. **c)** Burst features are highlighted in the left inset: burst duration (BD), and inter-spike intervals (ISI); box plots show IBI **(c)**, BD **(d)**, and ISI **(e)** for experimental traces presented in **(b)** in black, and maroon circles show simulated results. Error bars show minimum and maximum of the distribution for a 10 sec recording period.

Figure 5. Physiological consequences of I_{NaP} on neural discharge. a) Simulated membrane voltage for increasing values of, g_{NaP}, and its effect on burst discharge; Value of 1x g_{NaP} was chosen to match experimental data in **(b)**. **b)** Dynamic-clamp addition of I_{NaP} in an intrinsically bursting sensory neuron and its response to increases in g_{NaP}; Values of g_{NaP} used are 0.36 and 0.54 nS/pF for 1X and 1.5X respectively. The red double arrows highlight reduction in inter-burst interval (IBI) in both **(a)** and **(b)**. **c)** Burst features are highlighted in the left inset: burst duration (BD), and inter-spike intervals (ISI); IBI **(c)**, BD **(d)**, and, ISI **(e)** are shown for experimental traces presented in **(b)** in black; Maroon circles show simulated results. Error bars show minimum and maximum of the distribution for a 10 sec recording period.

Figure 6. Mechanism of action of I_{NaR} and I_{NaP} – Model analyses. a-c) The slow inactivation/recovery variable is overlaid (magenta) on membrane voltage traces (grey) under control **(a)**, increased g_{NaP} **(b)**, and increased g_{NaR} **(c)** conditions; The dark blue dashed lines in **(a-c)** indicate the maximum and minimum values of the persistent inactivation variable under control conditions; The light green arrow in **(b)**, highlights a reduced peak recovery required for burst onset; The light blue curvy arrows in **(b, c)** indicate reduced slow inactivation for burst termination. **d, e)** Bifurcation diagrams showing the steady-states and bursting regimes in the membrane voltage (V) and slow inactivation/recovery (h_p) phase plane. The red lines represent resting/quiescence states consistent with low values of h_p recovery. The meeting point of stable equilibria (red) and unstable equilibria (black solid lines) represents the theoretical threshold for burst onset (see **Supplementary Information**). The blue open circles are the unstable periodics that form region of attraction on either side of the stable equilibria for sub-threshold membrane voltage oscillations; The meeting point of the curve of unstable periodics with the stable periodics (green filled circles) represents the theoretical threshold for burst offset/termination (see **Supplementary Information**). The dashed boxes in **(d)** and **(e)** highlight shifts in burst offset thresholds due to increases

in g_{NaR} **(d)** and g_{NaP} **(e)**; brown dashed arrows in **(e)** highlight shifts in burst onset thresholds due to g_{NaP} increases; 1X g_{NaR} = 3.3 nS/pF and 1X g_{NaP} = 0.5 nS/pF.

Figure 7. Resurgent Na^+ current stabilizes burst discharge and confers noise tolerance. a - c) Simulated membrane voltage shows neural activity patterns without any g_{NaR} **(a)**, with added white noise input **(b)**, and with subsequent addition of g_{NaR} **(c)**. Expanded regions in **(a-c)** show membrane voltage sub-threshold oscillations (STO) during an inter-burst interval. Also overlaid is the evolution of the slow sodium inactivation/recovery variable; Arrow indicates recovery during IBI, and magenta circle marks an arbitrary time point used to track these trajectories in **(d - f)**. **d - f)** Bifurcation diagrams with projected trajectories of (h_p, V), shown in magenta to highlight the effect of addition of noise near sub-threshold voltages **(e)** and then the enlarged region of noise tolerance (highlighted green shaded region) due to addition of g_{NaR} in **(f)**. The magenta circle marks the beginning time points of each trajectory.

Figure 8. Resurgent Na^+ current reduces entropy in neural discharge. a - b) Schematic showing introduction of random noise input along with a depolarizing step current to disrupt rhythmic bursting in the model neuron and during dynamic-clamp experiments **(b)**; In **(a)**, I_{stim} is the sum of the constant step input and random white noise, and in **(b)**, I_{dyn} is the sum of step, random noise and I_{NaR}. **c – d)** Raster plots showing patterns of inter-event intervals (IEIs) for the different conditions shown in the model **(e)**, and during real-time dynamic-clamp **(f)**. **e – f)** Time series of Log_{10}(IEI) for the different conditions shown in the model **(e)**, and during real-time dynamic-clamp **(f)**. **g – h)** Shannon entropy (H) and coefficient of variability (CV) measured for IEIs under the different conditions presented in **(c)** and **(d)**. Plotted circles for the model represent an average across 10 trials, while individual trials are presented for the data points from two cells. In both **(g)** and **(h)**, C: control, N: after addition of random noise, 1X and 2X are supplements in g_{NaR} values.

Figure 9. A consolidated role for Na^+ currents in information processing. a) A sinusoidal ZAP current input of increasing frequencies from 1 – 250 Hz over 10 sec. **b)** Sub-threshold voltage response showing resonant behavior that is enhanced by increasing g_{NaP} (blue traces). **c)** Upper trace: membrane resonance in the presence of ambient noise that can increase the likelihood of near-threshold behavior (arrows indicate noise-induced heightened response); Lower trace: presence of noise increases uncertainty in neural discharge **d)** Noise tolerance due to g_{NaR} returns order of bursts.

Supplementary Information

4 Supplementary figures and legends
1 Table
1 piece of Supplementary information providing the *Model analyses using dynamical systems methods*
2 pieces of Supplementary information providing the *Model code as MATLAB scripts*
3 pieces of Supplementary information providing the *Dynamic-clamp C^{++} code*

Acknowledgements

Grant support include NIH/NINDS NS095157 (SV); NIH/NINDS NS07134 and UCLA Faculty Research Grant (SHC); NSF DMS1410935 (DHT); NIH/NHLBI 1R01HL134346 (RO); The David Vickter, The

Toeffler Family & Simon-Strauss Foundations (MWP). We are grateful to Dr. Bruce Bean, Dr. Christopher Del Negro and Dr. Alan Garfinkel for helpful comments on an earlier version of the manuscript.

Online Methods

Neuron model for bursting activity

The conductance-based Mes V neuron model that we use to investigate the physiological role for I_{NaR} and I_{NaP} components of I_{Na} in burst discharge, incorporates a minimal set of key ionic conductances essential for producing rhythmic bursting and for maintaining cellular excitability in these neurons [7]. These include: 1) a potassium leak current, I_{leak}, 2) sodium current, I_{Na} as described above, and, 3) a 4-AP sensitive delayed-rectifier type potassium current (I_K) [7, 31]. The model equations follow a conductance-based Hodgkin-Huxley formalism [12] and are as follows.

$$V' = \left(-I_{Na} - I_K - I_{leak} + I_{app}\right)/C$$

$$h_t' = \frac{ht_\infty(V) - h_t}{\tau_t}$$

$$h_p' = \frac{hp_\infty(V) - h_p}{\tau_p(V)}$$

$$b_r' = \alpha_b(1 - b_r)br_\infty(V) - k_b\beta_{br}(V)b_r$$

$$h_r' = \alpha_{hr}(V)hr_\infty(V) - 0.8\beta_{hr}(V)h_r$$

$$n' = \frac{n_\infty(V) - n}{\tau_n}$$

In what follows, we provide the formulation for each of the ionic currents and describe in detail, the novel I_{NaR} model.

A. *Voltage-gated sodium currents*

In vitro action potential clamp studies in normal mouse Mes V neurons, and voltage-clamp studies in Nav1.6 subunit SCN8a knockout mice have demonstrated existence of three functional forms of the total

408 sodium current, I_{Na}, including the transient (I_{NaT}), persistent (I_{NaP}) and resurgent (I_{NaR}) components [10,
409 13]. Each of these currents are critical for Mes V electrogenesis including burst discharge, however, their
410 exclusive role is yet unclear. Lack of suitable experimental model or manipulation to isolate each of these
411 TTX-sensitive components, led us to pursue an alternative approach involving computational model
412 development of the physiological I_{Na}. To further allow model-based experimental manipulation of
413 individual components of the I_{Na}, we designed a conductance-based model as follows. To satisfy a single
414 channel mediating all the three components, the equation for the total sodium current can be written as:

415 $$I_{Na} = I_{NaT} + I_{NaR} + I_{NaP}$$

416 where,

417 $$I_{NaT} = \boldsymbol{g_{NaT}}(m_{t\infty}(V)h_t)(V - E_{Na})$$

418 $$I_{NaR} = \boldsymbol{g_{NaR}}((1 - b_r)^3 h_r^5)(V - E_{Na})$$

419 $$I_{NaP} = \boldsymbol{g_{NaP}}\big(m_{p\infty}(V)h_P\big)(V - E_{Na})$$

420 The maximal persistent conductance, g_{NaP} was set 5-10% of the transient g_{NaT}[32] and the resurgent
421 was set to 15-30% of g_{NaT}, based on the relative percentage of maximum I_{NaR} and I_{NaT} as revealed by
422 voltage-clamp experiments (e.g., **Fig. 3)**; E_{Na} is the Na^+ reversal potential.

423 Based on experimental data, the gating function/variable, $m_{t\infty}(V)$, and h_t, for I_{NaT}, and, $m_{p\infty}(V)$,
424 and, h_P, for I_{NaP} are modeled as described in [7]. The rate equations for the inactivation gating variables h_t,
425 and, h_P, model the fast and slow inactivation of the transient and persistent components respectively. The
426 activation gates are steady-state voltage-dependent functions, consistent with fast voltage-dependent
427 activation of I_{Na}.

428 Steady-state voltage-dependent activation and inactivation functions of *transient* sodium current
429 respectively include:

$$mt_\infty(V) = \frac{1}{1+e^{\left(-(V+35)/4.3\right)}}; \quad ht_\infty(V) = \frac{1}{1+e^{\left((V+55)/7.1\right)}}$$

Steady-state activation, inactivation and steady-state voltage-dependent time constant of inactivation for *persistent* sodium current respectively include:

$$mp_\infty(V) = \frac{1}{1+e^{\left(-(V+50)/6.4\right)}}; \quad hp_\infty(V) = \frac{1}{1+e^{\left((V+52)/14\right)}}; \tau_p(V) = 100 + \frac{10000}{1+e^{\left((V+60)/10\right)}}$$

The novel I_{NaR} formulation encapsulates the block/unblock mechanism using a block/unblock variable (b_r), and, a second hypothetical variable for a competing inactivation, which we call, h_r. We call this a *hybrid* model, to highlight the fact that the model implicitly incorporates the history or state-dependent eccentric sodium resurgence, following a transient channel opening, and combines this into a traditional Hodgkin-Huxley type conductance-based formulation. In the b_r' and h_r' rate equations for b_r, and, h_r, the block/unblock variable, b_r increases or grows according to the term, $\alpha_b(1-b_r)br_\infty(V)$, and decays as per the term, $k_b\beta_{br}(V)b_r$, described as follows:

$\boldsymbol{\alpha_b(1-b_r)br_\infty(V)}$: In this growth term, we incorporate state-dependent increase in b_r, as follows; we assume that the rate of increase in b_r is proportional to the probability of channels currently being in the open state, with a rate constant, α_b which we call 'rate of unblocking'; such probability is a function of the membrane voltage given by, $br_\infty(V)$, defined as below:

$$br_\infty(V) = \frac{1}{1+e^{\left((V+40)/12\right)}}$$

The term $\left(1-br_\infty(V)\right)$, models the steady-state voltage-dependency guiding the unblocking process. The channels being in open state is represented by the term, $(1-b_r)$. Note that if $(1-b_r)$ is close to 1, this means that larger proportion of channels are in an open state, and therefore b_r grows faster, promoting blocking. We modeled $br_\infty(V)$ as a decreasing sigmoid function, such that, at negative

membrane potentials, channels have a high probability to enter future depolarized states and therefore, $(1 - b_r) \sim 0$, in turn, b_r does not grow fast.

$\boldsymbol{k_b \beta_{br}(V) b_r}$**:** In this decay term, we assume that the rate of decay of b_r, is proportional to the probability of channels being in the blocked state, with a constant of proportionality k_b, and, this probability is given by a voltage-dependent function, $\beta_{br}(V)$, defined as below:

$$\beta_{br}(V) = \frac{2}{1 + e^{\left(-(V-40)/8\right)}}$$

Note that, $\beta_{br}(V)$ gives a high probability at depolarized potentials, indicating a blocked state and enables decrease in b_r in subsequent time steps.

Taken together, b_r, represents a mechanistic implementation of a block/unblock process by a blocking particle (see schematic of channel gating in **Fig. 3a**). Additionally, a hypothetical competing inactivation variable, h_r, sculpts the voltage-dependent rise and decay times and peak amplitude of sodium resurgence at -40 mV following a brief depolarization (i.e., transient activation), as observed in voltage-clamp experiments (see **Fig. 3b**). The functions, $\alpha_{hr}(V), \beta_{hr}(V)$ and $hr_\infty(V)$ are defined as voltage-dependent rate equations that guide the voltage-dependent kinetics and activation/inactivation of the I_{NaR} component as given below.

The steady-state voltage-dependency of the competing inactivation necessary to generate a *resurgent* Na^+ current is defined as follows:

$$hr_\infty(V) = \frac{1}{1+e^{\left((V+40)/20\right)}}$$

The voltage-dependent rate functions of such inactivation is defined by two functions as follows:

$$\alpha_{hr}(V) = \frac{1}{1+e^{\left(-(V+45)/11\right)}}; \qquad \beta_{hr}(V) = \frac{0.5}{1+e^{\left(-(V+40)/15\right)}}$$

470 The steepness of the voltage-dependent sigmoid functions for activation and inactivation were tuned
471 to obtain the experimentally observed I_{NaR} activation (see **Fig. 3**; also see [10, 13, 16]). To obtain the kinetics
472 (rise and decay times) of I_{NaR} comparable to those observed during voltage-clamp experiments (see
473 **Supplementary Fig. 3**), the model required three units for the blocking variable ($(1 - b_r)^3$) and five units
474 for the inactivation variable ($h_r{}^5$) (see I_{NaR} equation). Together, the modeled I_{Na} reproduced the key
475 contingencies of the Nav1.6 sodium currents (see **Supplementary Fig. 2**) [11, 15, 16].

476 Sensitivity analyses was conducted for the key parameters of I_{NaR} gating including α_b, and, k_b. Note
477 that these two parameters control the rate of blocking. As expected, increasing α_b, that controls rate of
478 increase in b_r, decreased the peak amplitude of I_{NaR}, similar to an experimental increase in block efficacy
479 by a β-peptide (e.g., [14]). On the other hand, k_b also moderates b_r, and increasing k_b, enhances b_r decay
480 rate, that significantly enhanced I_{NaR}, and, therefore burst duration (not shown). Large increases in k_b
481 significantly enhanced I_{NaR} , and indeed transformed bursting to high frequency tonic spiking. However,
482 the effects of I_{NaR} on bursting described in the results section were robust for a wide range of values of
483 these parameters (>100% increase from default values), and, for our simulations, the range of values, $\alpha_b =$
484 $0.08\ to\ 0.1$, $k_b = 0.8\ to\ 1.2$, were used to reproduce Mes V neuron discharge properties. To reproduce
485 experimentally observed spike width, we additionally tuned the inactivation time constant, $\tau_t = 1.5 \pm$
486 0.5, for I_{NaT}.

487 ***B.*** *Potassium and leak currents*

488 The 4-AP sensitive delayed-rectifier type potassium current, I_K, and the leak current, I_{leak} were
489 modeled similar to [7] as below; also see [31].

490 $$I_K = g_K n(V - E_K)$$

491 $$I_{leak} = g_{leak}(V - E_{leak})$$

492 where, the steady-state voltage-dependent activation function for the gating variable, n is given as:

493 $$n_\infty(V) = \frac{1}{1 + e^{\left(-(V-43)/3.9\right)}}$$

494 E_K and E_{leak} are K^+ and leak reversal potentials respectively. Model parameter values used are provided
495 in **Table. 1**.

496 ***Brain slice preparation***

497 All animal experiments were performed in accordance to the institutional guidelines and regulations
498 using protocols approved by Animal Research Committee at UCLA. Experiments were performed in P8-
499 P14 wild-type mice of either sex. Mice were anesthetized by inhalation of isofluorane and then
500 decapitated. The brainstem was extracted and immersed in ice-cold cutting solution. The brain-cutting
501 solution used during slice preparation was composed of the following (in mM): 194 Sucrose, 30 NaCl, 4.5
502 KCl, 1.2 NaH_2PO_4, 26 $NaHCO_3$, 10 glucose, 1 $MgCl_2$. The extracted brain block was mounted on a
503 vibrating slicer (DSK Microslicer, Ted Pella) supported by an agar block. Coronal brainstem sections
504 consisting of rostro-caudal extent of Mes V nucleus, spanning midbrain and pons were obtained for
505 subsequent electrophysiological recording.

506 ***Voltage-clamp electrophysiology***

507 To obtain direct experimental data to drive I_{NaR} model development, we performed voltage-clamp
508 experiments on Mes V neurons and recorded Na^+ currents by blocking voltage-gated K^+ and Ca^{2+} currents
509 similar to [10]. The pipette internal solution contained the following composition (in mM): 130 CsF, 9 NaCl,
510 10 HEPES, 10 EGTA, 1 $MgCl_2$, 3 K_2-ATP, and 1 Na-GTP. The external recording solution contained the
511 following composition (in mM): 131 NaCl, 10 HEPES, 3 KCl, 10 glucose, 2 $CaCl_2$, 2 $MgCl_2$, 10
512 tetraethylammonium (TEA)-Cl, 10 CsCl, 1 4-aminopyridine (4-AP), and 0.3 $CdCl_2$. The voltage-clamp
513 protocol consisted of a holding potential of -90 mV followed by a brief voltage pulse (3 ms) of +30 mV,

514 to remove voltage-dependent block, followed by voltage steps between -70 mV to -10 mV, in steps of 10
515 mV for ~ 100 ms to activate I_{NaR}, and then returned to -90 mV. A 0.5 μM TTX abolished the Na^+ current
516 and the residual leak current was subtracted to isolate evident sodium currents. Recordings with series
517 $R_{series} > 0.1R_m$ were discarded.

518 ***Dynamic-clamp electrophysiology***

519 Real-time dynamic-clamp electrophysiology and *in vitro* current-clamp recording were used for
520 testing the physiological effects of Na^+ currents on burst discharge as well as noise-mediated entropy
521 changes corrected by I_{NaR} [33]. We selected neurons responding with a bursting pattern in response to supra-
522 threshold step current injection in the Mes V nucleus in brainstem slice preparation for our study; >50%
523 of neurons showing other patterns (e.g., tonic or single spiking cells) were discarded. Dynamic-clamp was
524 successfully performed in bursting cells (n = 10). For dynamic-clamp recording, slices were placed in
525 normal ACSF at room temperature (22–25°C). The ACSF recording solution during patch-clamp
526 recording consisted of the following (in mM): 124 NaCl, 4.5 KCl, 1.2 NaH_2PO_4, 26 $NaHCO_3$, 10 glucose,
527 2 $CaCl_2$, 1 $MgCl_2$. Cutting and recording solutions were bubbled with carbogen (95% O_2, 5% CO_2) and
528 maintained at pH between 7.25 – 7.3. The pipette internal solution used in current clamp experiments was
529 composed of the following (in mM): 135 K-gluconate, 5 KCl, 0.5 $CaCl_2$, 5 HEPES (base), 5 EGTA, 2 Mg-
530 ATP, and 0.3 Na-ATP with a pH between 7.28 – 7.3, and osmolarity between 290 ± 5 mOsm. Patch
531 pipettes (3 – 5 MΩ) were pulled using a Brown/Flaming P-97 micro pipette puller (Sutter Instruments).
532 Slices were perfused with oxygenated recording solution (~2ml/min) at room temperature while secured
533 in a glass bottom recording chamber mounted on an inverted microscope with differential interface
534 contrast optics (Zeiss Axiovert 10). Current clamp (and dynamic-clamp) data were acquired and analyzed
535 using custom-made software (G-Patch, Analysis) with sampling frequency: 10 kHz; cut-off filter
536 frequency: 2 kHz.

537 The Linux-based Real-Time eXperimental Interface (RTXI v1.3) was used to implement dynamic-
538 clamp , running on a modified Linux kernel extended with the Real-Time Applications Interface, which
539 allows high-frequency, periodic, real-time calculations [34]. The RTXI computer interfaced with the
540 electrophysiological amplifier (Axon Instruments Axopatch 200A, in current-clamp mode) and the data
541 acquisition PC, via a National Instruments PCIe-6251 board. Computation frequency was 20 kHz.

542 The model I_{NaR} current used for real-time dynamic clamping into Mes V neuron *in vitro* was
543 developed as discussed above. The ionic conductance g_{NaR} was set to suitable values to introduce model
544 I_{NaR} current into a Mes V neuron during whole-cell current-clamp recording. For experiments involving
545 noise modulation, two approaches were used to model random noise generated in RTXI: 1) using a
546 Wiener-like process with normally distributed random values, 2) normally-distributed random numbers
547 were generated from uniformly-distributed numbers using the central limit theorem:

548 $$N(t) = \left(\sum_{i=1}^{12} U_i\right) - 6$$

549 where, $N(t)$ is a normally-distributed random number with mean, $\mu = 0$, and standard deviation, $\sigma = 1$,
550 each U_i is a uniformly-distributed random number between 0 - 1 generated using the C^{++} rand() function.
551 A current, I_{noise} was then generated as follows:

552 $$I_{noise}(t) = I_{noise}(t-1) + N(t) \cdot \sqrt{\Delta_t} \cdot A$$

553 where, $N(t)$ is a uniformly-distributed random number between 0 - 1 generated in C^{++} at each sampling
554 time t and Δ_t is the time distance between consecutive computations. In both the above cases, A is a
555 scaling factor representing maximal peak-to-peak noise amplitude, modified to adjust noise amplitudes
556 suitably to produce discernable burst irregularities. Values of A were set during experimentation and
557 ranged from 3 - 5 across various cells for the data presented. $I_{noise}(t)$ was injected as pA current.

558 ***Model simulation and Data analyses***

Model simulation and all the analyses were performed using MATLAB (Mathworks™) (see model code provided as **Supplementary Information**). Model bifurcation analyses were performed using XPPAUT/AUTO [35]; A variable step Runge-Kutta method 'ode45' was used for current-clamp simulations and 'ode23s' was used for voltage-clamp simulations.

Inter-event intervals (IEI) between spikes in dynamic-clamp recordings were detected using Clampfit 9.0 software and were classified *post hoc* as ISIs and IBIs based on a bi-modal distribution of IEIs. Typically, IEI values < 40 ms were considered as ISIs within bursts and IEI values ≥ 40 ms were considered as IBIs. Any occasional isolated spikes were eliminated from analyses for burst duration calculations.

To calculate Shannon's entropy[36] in the inter-event intervals (IEIs), we generated histograms of and calculated the probabilities for each bin of the underlying IEI distributions for each 10 sec spike trains. The probability of kth IEI bin from a distribution of n equal size bins was calculated from the bin counts, $N(k)$ as:

$$p(k) = \frac{N(k)}{\sum_{k=1}^{n} N(k)}$$

The entropy, H was calculated using the following formula:

$$H = -\sum_{k=1}^{n} p_k \log_2 p_k$$

where, n is the total number of IEI bins, each with probability, p_k.

The coefficient of variation (CV) in IEIs was calculated as follows:

$$CV = \frac{s}{\bar{x}}$$

where, s is the IEI sample standard deviation, and, $\bar{x}$ is the sample mean.

579 **References**

580 1. Krahe, R. & Gabbiani, F. Burst firing in sensory systems. *Nat Rev Neurosci* **5**, 13-23 (2004).
581 2. Ermentrout, B.G. & Terman, D.H. Bursting Oscillations. in *Mathematical Foundations of Neuroscience*
582 103-127 (Springer-Verlag New York, 2010).
583 3. Del Negro, C.A., Hsiao, C.F., Chandler, S.H. & Garfinkel, A. Evidence for a novel bursting mechanism in
584 rodent trigeminal neurons. *Biophys J* **75**, 174-182 (1998).
585 4. Bialek, W., Rieke, F., de Ruyter van Steveninck, R.R. & Warland, D. Reading a neural code. *Science* **252**,
586 1854-1857 (1991).
587 5. Catterall, W.A. From ionic currents to molecular mechanisms: the structure and function of voltage-gated
588 sodium channels. *Neuron* **26**, 13-25 (2000).
589 6. Alonso, A. & Llinás, R.R. Subthreshold Na+-dependent theta-like rhythmicity in stellate cells of entorhinal
590 cortex layer II. *Nature* **342**, 175-177 (1989).
591 7. Wu, N.*, et al.* Persistent sodium currents in mesencephalic v neurons participate in burst generation and
592 control of membrane excitability. *J Neurophysiol* **93**, 2710-2722 (2005).
593 8. Hutcheon, B. & Yarom, Y. Resonance, oscillation and the intrinsic frequency preferences of neurons.
594 *Trends Neurosci* **23**, 216-222 (2000).
595 9. Schwindt, P.C. & Crill, W.E. Amplification of synaptic current by persistent sodium conductance in apical
596 dendrite of neocortical neurons. *J Neurophysiol* **74**, 2220-2224 (1995).
597 10. Enomoto, A., Han, J.M., Hsiao, C.F., Wu, N. & Chandler, S.H. Participation of sodium currents in burst
598 generation and control of membrane excitability in mesencephalic trigeminal neurons. *J Neurosci* **26**, 3412-3422
599 (2006).
600 11. Raman, I.M. & Bean, B.P. Resurgent sodium current and action potential formation in dissociated
601 cerebellar Purkinje neurons. *J Neurosci* **17**, 4517-4526 (1997).
602 12. Hodgkin, A.L. & Huxley, A.F. A quantitative description of membrane current and its application to
603 conduction and excitation in nerve. *J Physiol* **117**, 500-544 (1952).
604 13. Enomoto, A., Han, J.M., Hsiao, C.F. & Chandler, S.H. Sodium currents in mesencephalic trigeminal
605 neurons from Nav1.6 null mice. *J Neurophysiol* **98**, 710-719 (2007).
606 14. Grieco, T.M., Malhotra, J.D., Chen, C., Isom, L.L. & Raman, I.M. Open-channel block by the cytoplasmic
607 tail of sodium channel beta4 as a mechanism for resurgent sodium current. *Neuron* **45**, 233-244 (2005).
608 15. Smith, M.R., Smith, R.D., Plummer, N.W., Meisler, M.H. & Goldin, A.L. Functional analysis of the mouse
609 Scn8a sodium channel. *J Neurosci* **18**, 6093-6102 (1998).
610 16. Raman, I.M. & Bean, B.P. Inactivation and recovery of sodium currents in cerebellar Purkinje neurons:
611 evidence for two mechanisms. *Biophys J* **80**, 729-737 (2001).
612 17. Khaliq, Z.M., Gouwens, N.W. & Raman, I.M. The contribution of resurgent sodium current to high-
613 frequency firing in Purkinje neurons: an experimental and modeling study. *J Neurosci* **23**, 4899-4912 (2003).
614 18. Kim, J.H., Kushmerick, C. & von Gersdorff, H. Presynaptic resurgent Na+ currents sculpt the action
615 potential waveform and increase firing reliability at a CNS nerve terminal. *J Neurosci* **30**, 15479-15490 (2010).
616 19. Birmingham, J.T., Szuts, Z.B., Abbott, L.F. & Marder, E. Encoding of muscle movement on two time scales
617 by a sensory neuron that switches between spiking and bursting modes. *J Neurophysiol* **82**, 2786-2797 (1999).
618 20. Zheng, Y. & Escabí, M.A. Proportional spike-timing precision and firing reliability underlie efficient
619 temporal processing of periodicity and envelope shape cues. *J Neurophysiol* **110**, 587-606 (2013).
620 21. Reich, D.S., Mechler, F., Purpura, K.P. & Victor, J.D. Interspike intervals, receptive fields, and information
621 encoding in primary visual cortex. *J Neurosci* **20**, 1964-1974 (2000).
622 22. Tiesinga, P., Fellous, J.M. & Sejnowski, T.J. Regulation of spike timing in visual cortical circuits. *Nat Rev*
623 *Neurosci* **9**, 97-107 (2008).
624 23. Mainen, Z.F. & Sejnowski, T.J. Reliability of spike timing in neocortical neurons. *Science* **268**, 1503-1506
625 (1995).
626 24. Raman, I.M., Sprunger, L.K., Meisler, M.H. & Bean, B.P. Altered subthreshold sodium currents and
627 disrupted firing patterns in Purkinje neurons of Scn8a mutant mice. *Neuron* **19**, 881-891 (1997).

628 25. Vilin, Y.Y. & Ruben, P.C. Slow inactivation in voltage-gated sodium channels: molecular substrates and
629 contributions to channelopathies. *Cell Biochem Biophys* **35**, 171-190 (2001).
630 26. Béhuret, S., Deleuze, C. & Bal, T. Corticothalamic Synaptic Noise as a Mechanism for Selective Attention
631 in Thalamic Neurons. *Front Neural Circuits* **9**, 80 (2015).
632 27. Faisal, A.A., Selen, L.P. & Wolpert, D.M. Noise in the nervous system. *Nat Rev Neurosci* **9**, 292-303
633 (2008).
634 28. Izhikevich, E.M., Desai, N.S., Walcott, E.C. & Hoppensteadt, F.C. Bursts as a unit of neural information:
635 selective communication via resonance. *Trends Neurosci* **26**, 161-167 (2003).
636 29. Lisman, J.E. Bursts as a unit of neural information: making unreliable synapses reliable. *Trends Neurosci*
637 **20**, 38-43 (1997).
638 30. Koch, C. & Segev, I. The role of single neurons in information processing. *Nat Neurosci* **3 Suppl**, 1171-
639 1177 (2000).
640 31. Del Negro, C.A. & Chandler, S.H. Physiological and theoretical analysis of K+ currents controlling
641 discharge in neonatal rat mesencephalic trigeminal neurons. *J Neurophysiol* **77**, 537-553 (1997).
642 32. Taddese, A. & Bean, B.P. Subthreshold sodium current from rapidly inactivating sodium channels drives
643 spontaneous firing of tuberomammillary neurons. *Neuron* **33**, 587-600 (2002).
644 33. Prinz, A.A., Abbott, L.F. & Marder, E. The dynamic clamp comes of age. *Trends Neurosci* **27**, 218-224
645 (2004).
646 34. Lin, R.J., Bettencourt, J., Wha Ite, J., Christini, D.J. & Butera, R.J. Real-time experiment interface for
647 biological control applications. *Conf Proc IEEE Eng Med Biol Soc* **2010**, 4160-4163 (2010).
648 35. Ermentrout, B. XPPAUT5.0 – the differential equations tool. (2001).
649 36. Shannon, C.E. & Weaver, W. *The Mathematical Theory of Communication* (University of Illinois Press,
650 Urbana, 1949).

651

Fig. 1. Study workflow

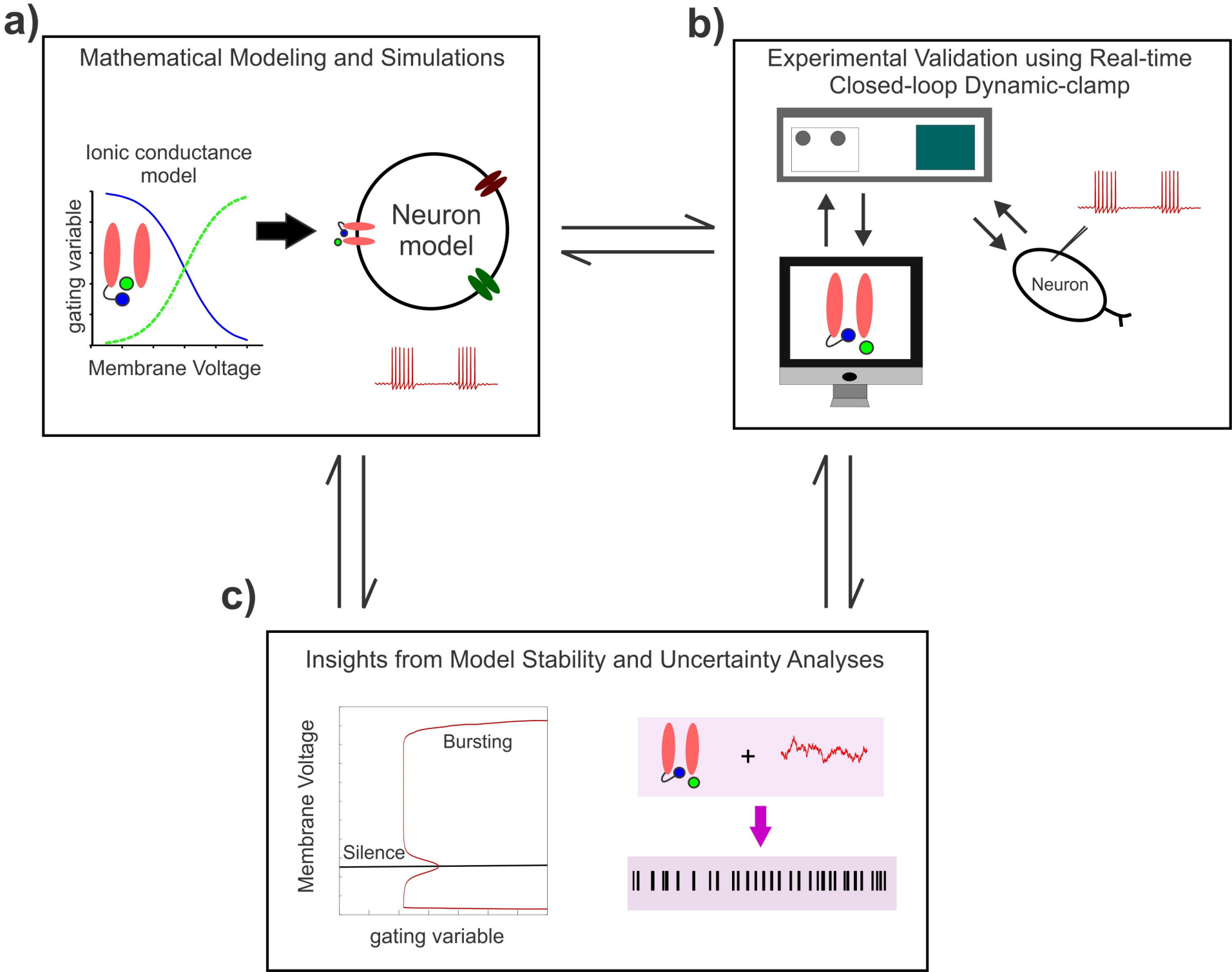

Fig. 2. Components of I_{Na}

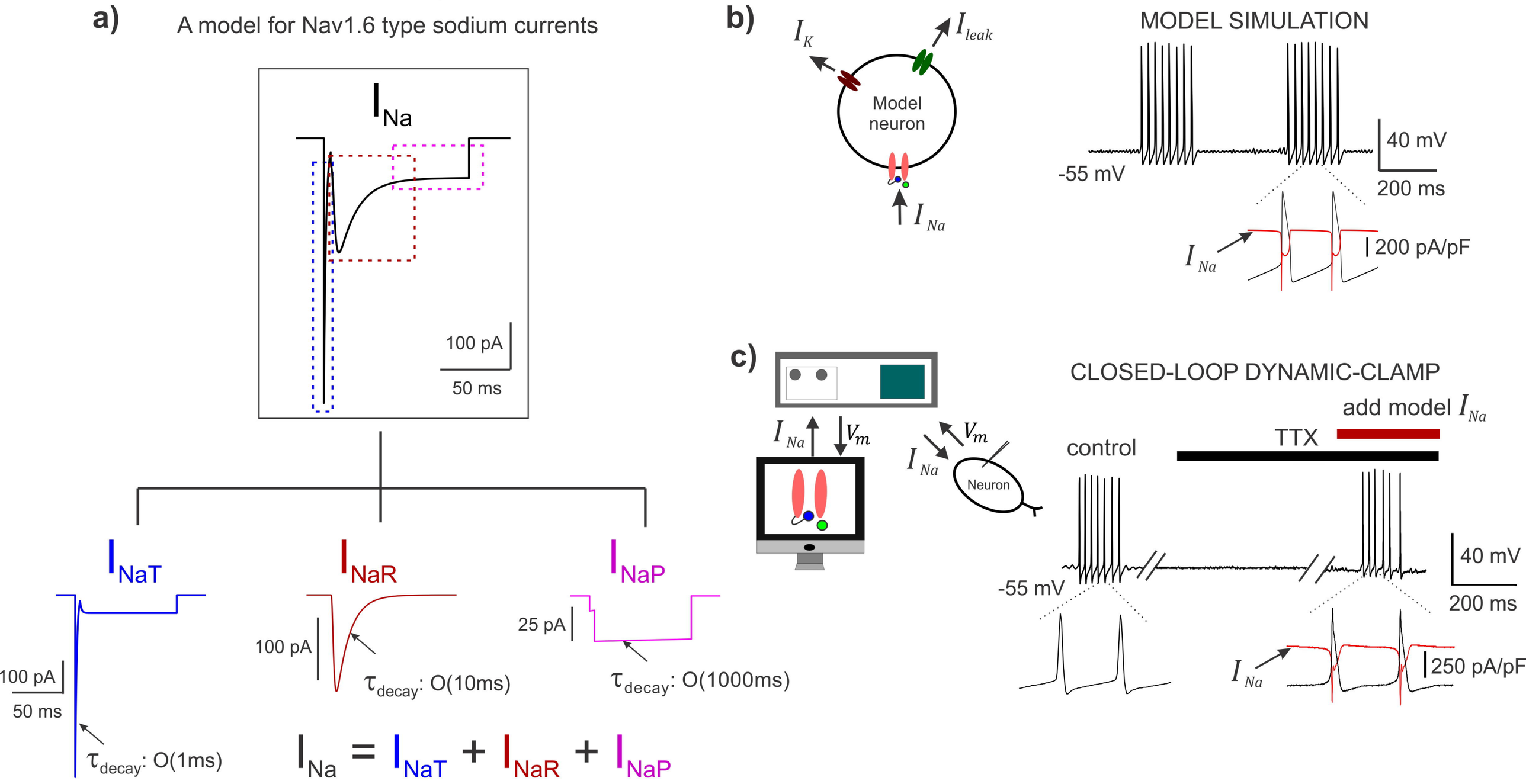

Fig. 3. A novel mathematical model for I_{NaR}

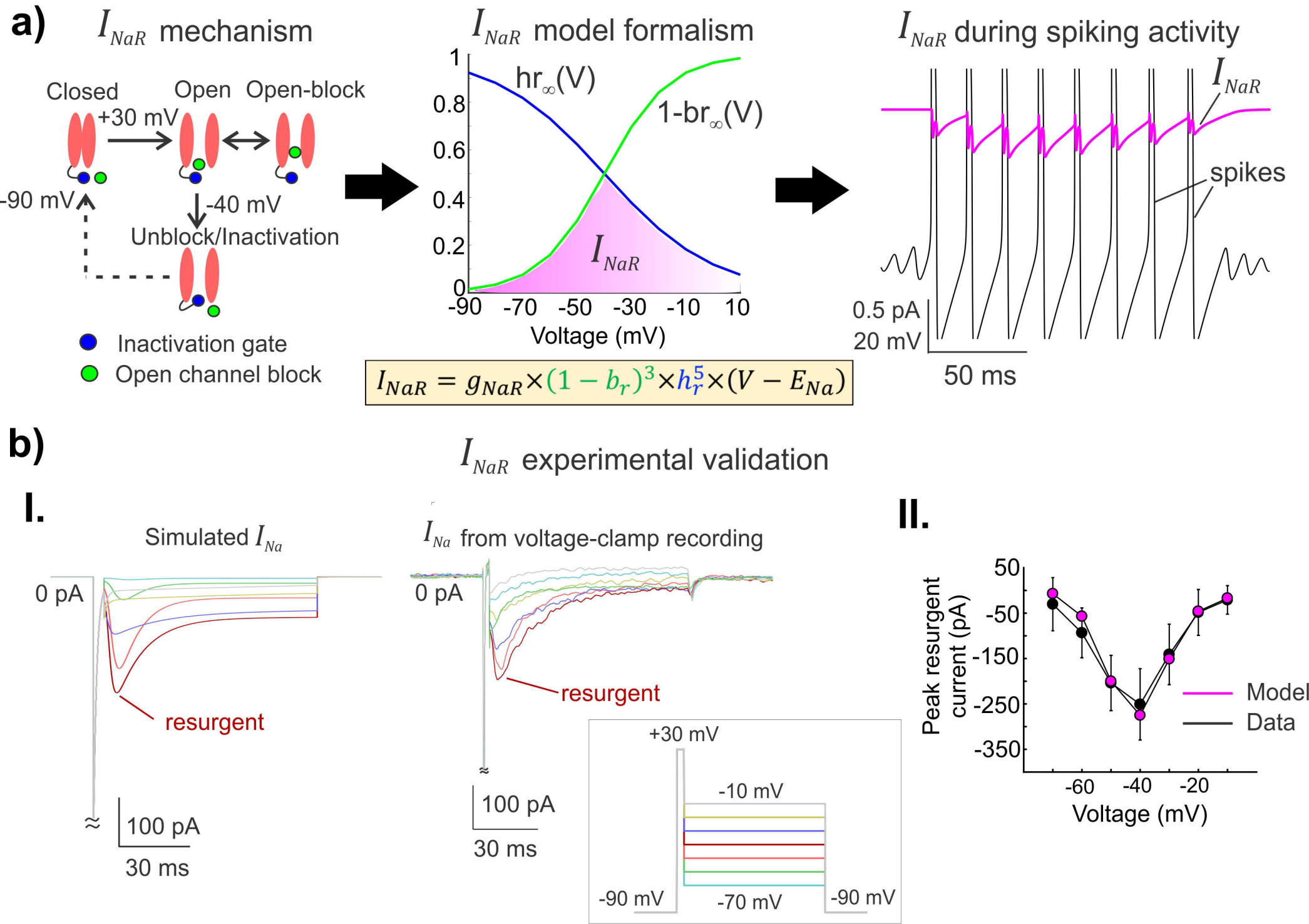

Fig. 4. I_{NaR} effects on burst discharge

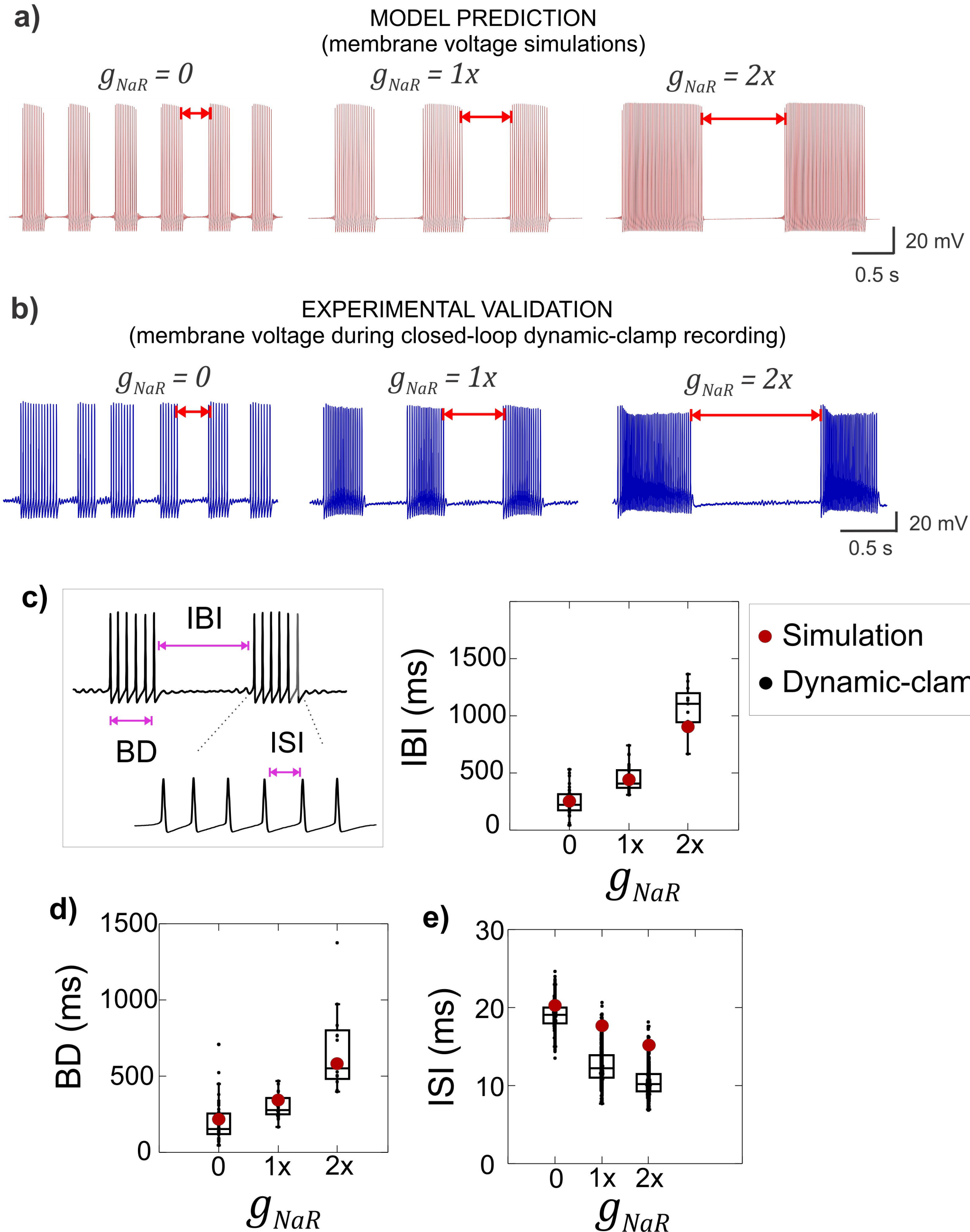

Fig. 5. I_{NaP} effects on burst discharge

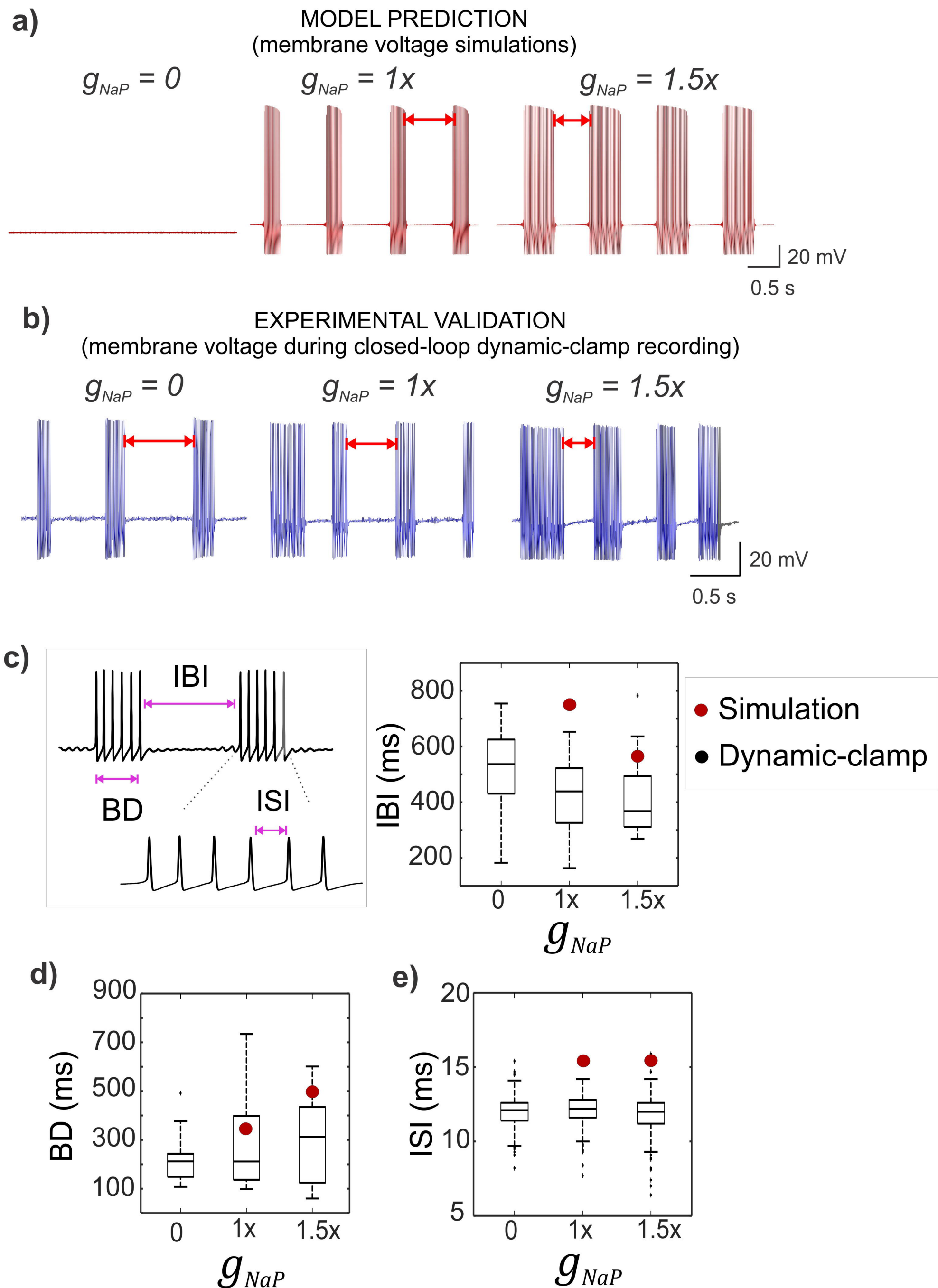

Fig. 6. I_{NaR} facilitates slow Na^+ inactivation

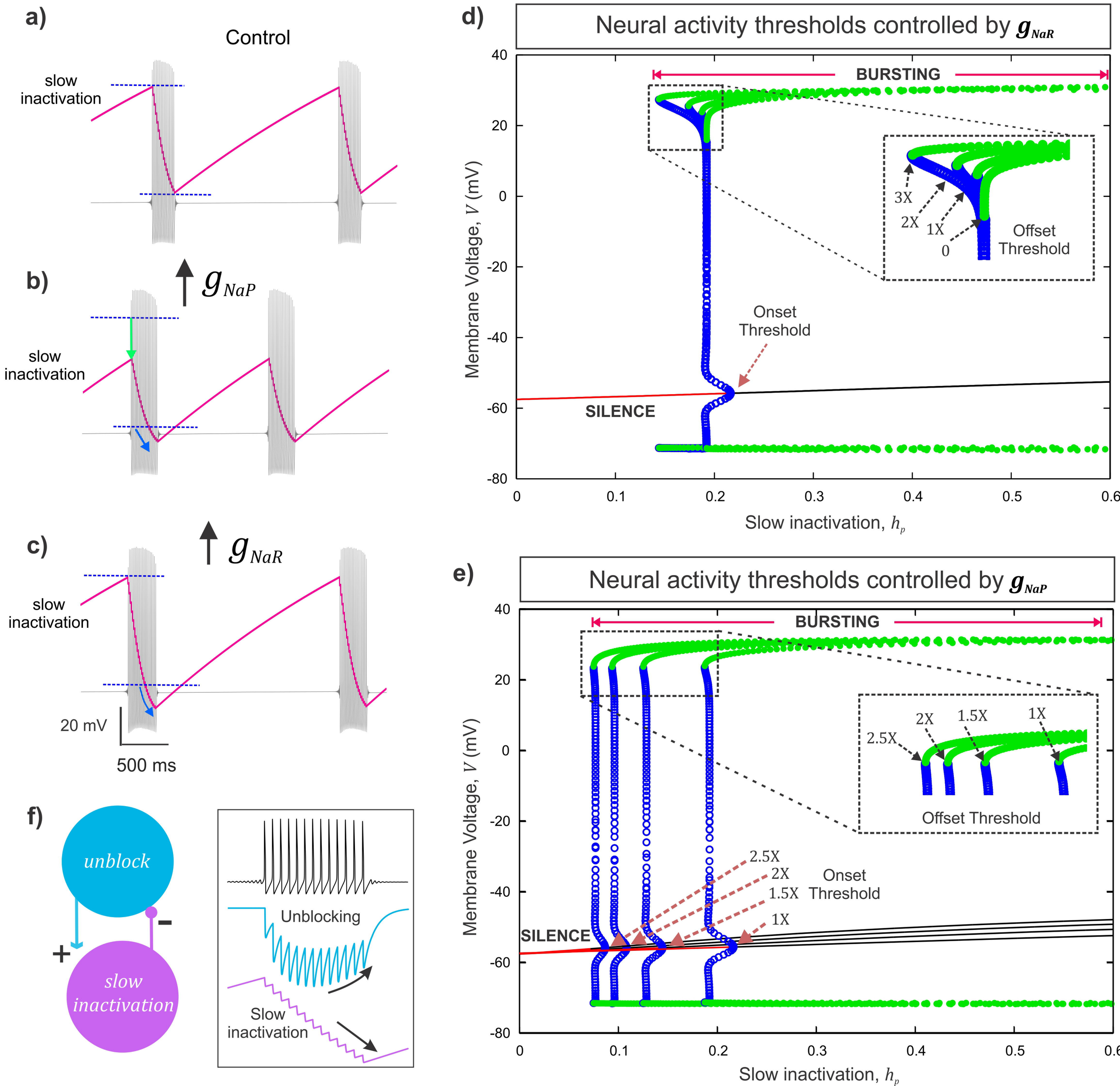

Fig. 7. Burst refractoriness and noise tolerance conferred by I_{NaR}

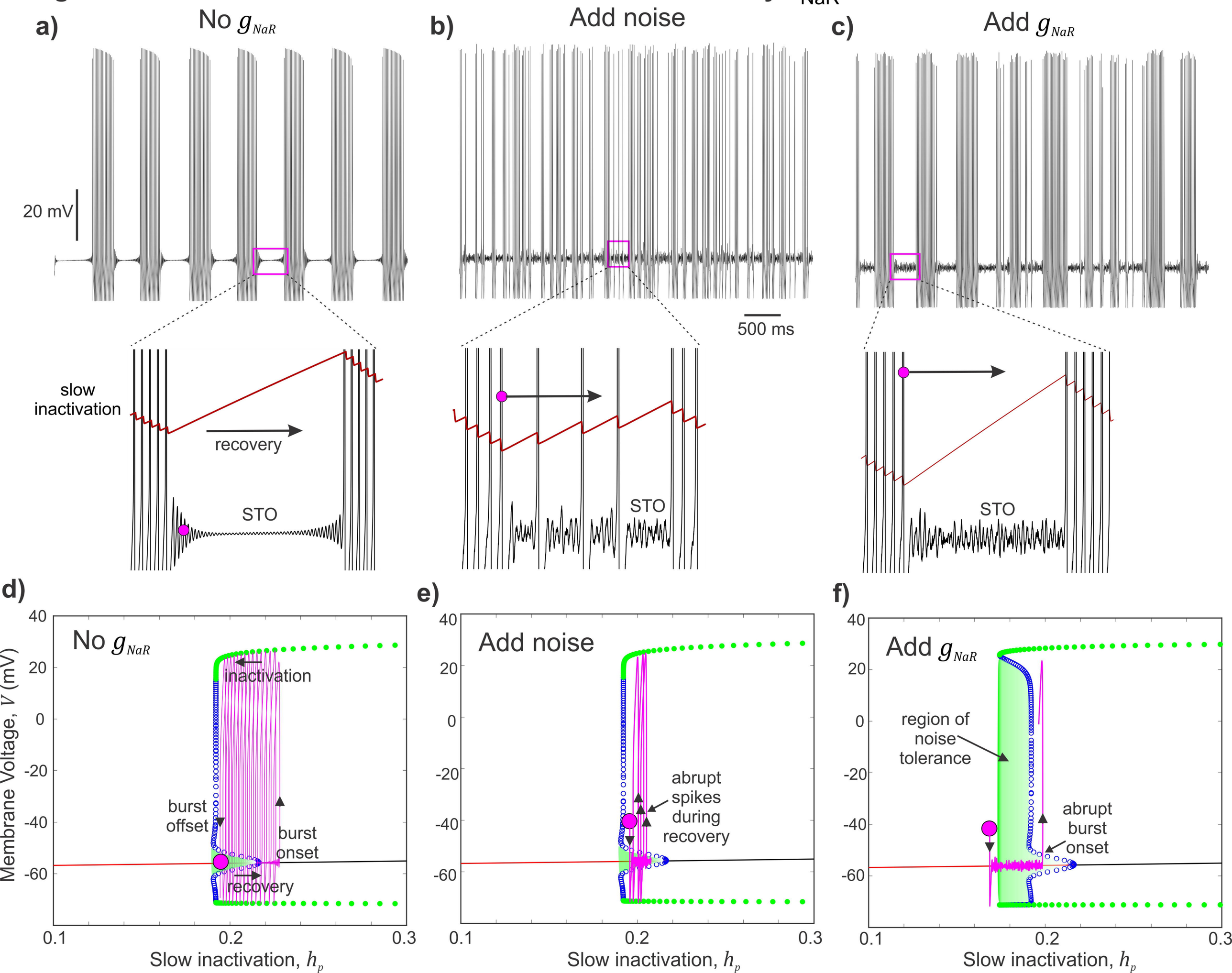

Fig. 8. I_{NaR} maintains order of bursts

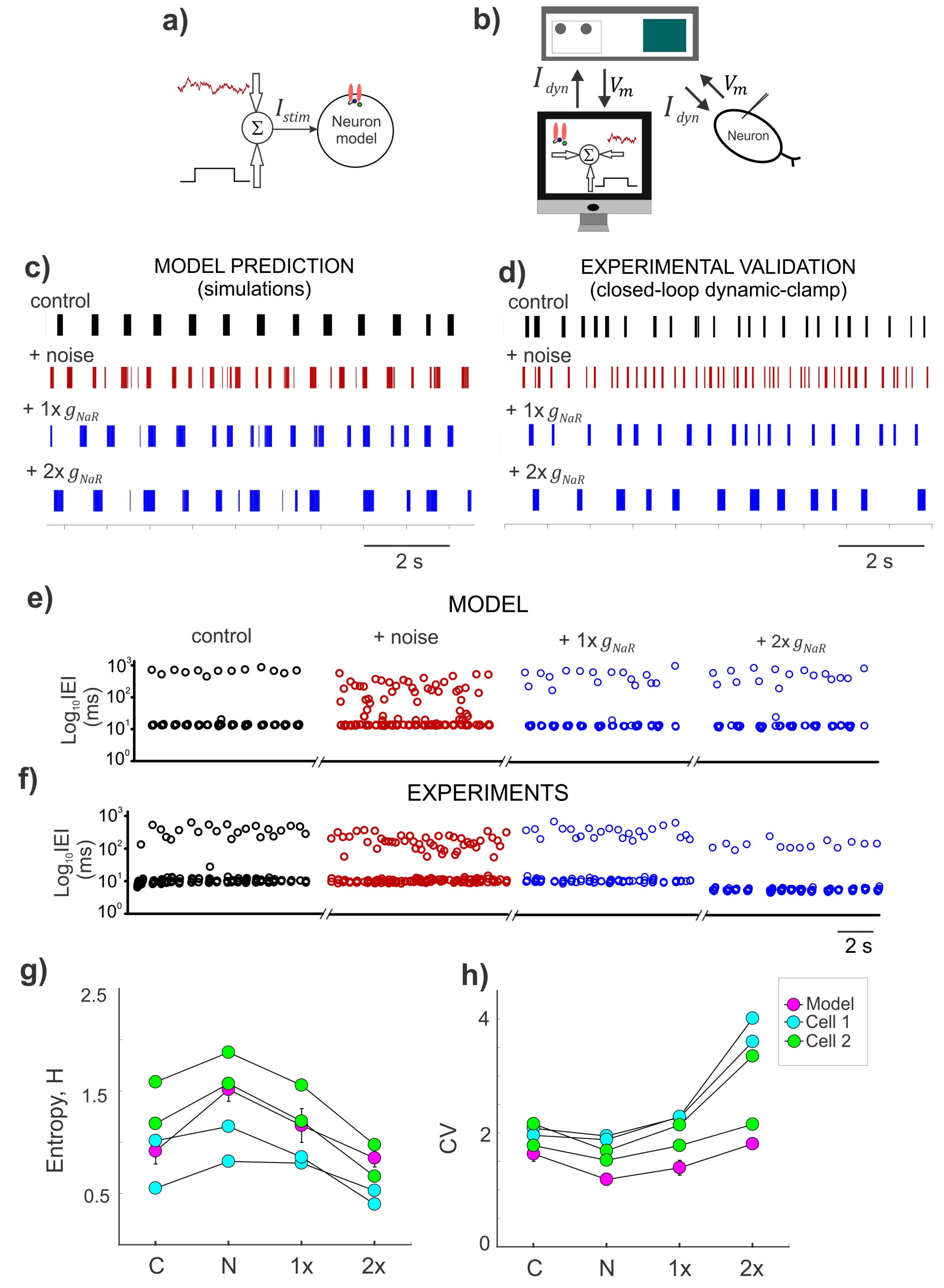
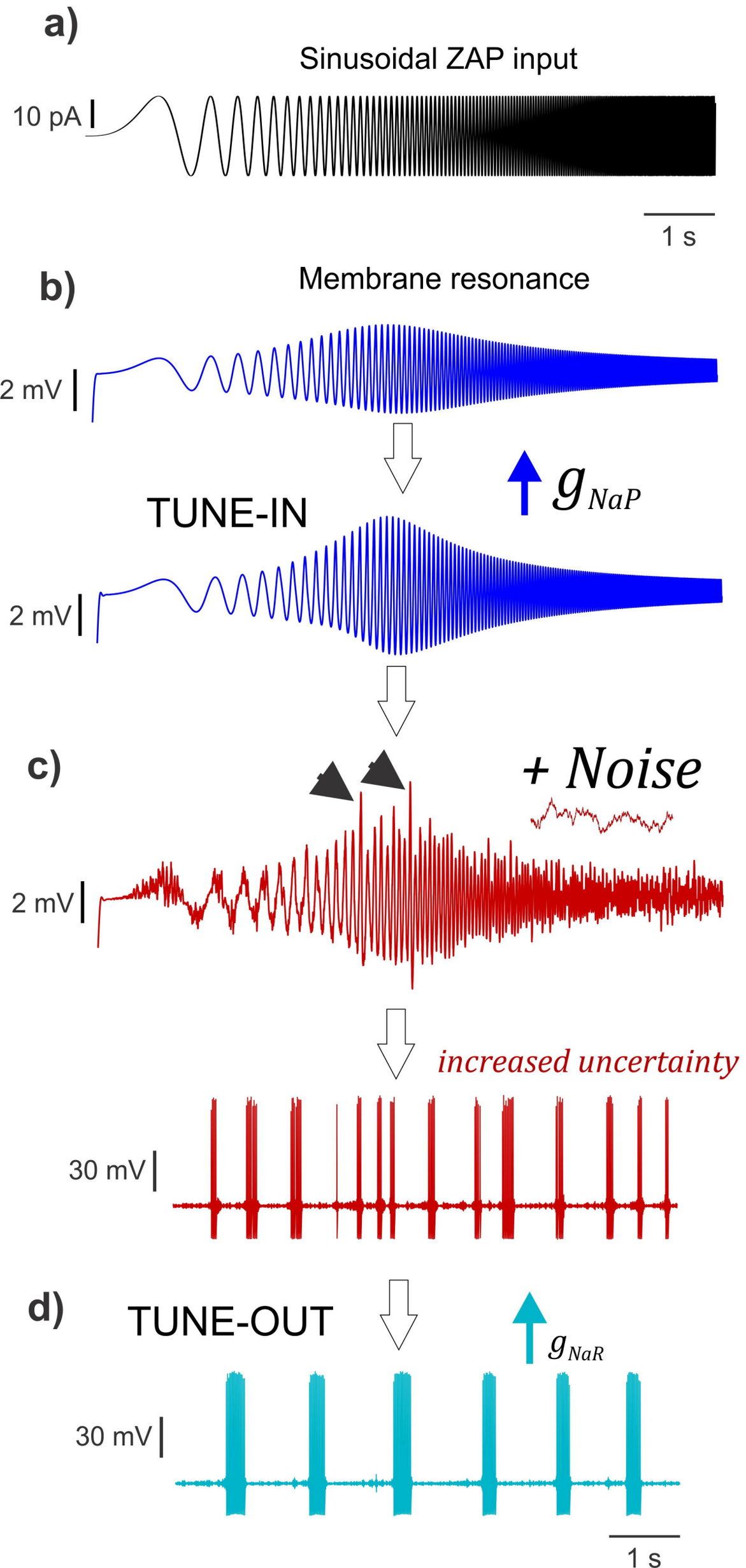
Fig. 9. A Tune-In-Tune-Out mechanism